



Article

Submarine and Subaerial Morphological Changes Associated with the 2014 Eruption at Stromboli Island

Daniele Casalbore ^{1,2,*}, Federico Di Traglia ³, Alessandro Bosman ², Claudia Romagnoli ⁴, Nicola Casagli ^{3,5} and Francesco Latino Chiocci ^{1,2}

¹ Dipartimento Scienze della Terra, Università Sapienza di Roma, Piazzale Aldo Moro 5, 00185 Rome, Italy; francesco.chiocci@uniroma1.it

² Istituto di Geologia Ambientale e Geoingegneria (IGAG), Consiglio Nazionale delle Ricerche, Struttura Congiunta DICEA, Via Eudossiana 18, 00184 Rome, Italy; alessandro.bosman@cnr.it

³ Dipartimento di Scienze della Terra, Università degli Studi di Firenze, Via La Pira 4, 50121 Firenze, Italy; federico.ditraglia@unifi.it (F.D.T.); nicola.casagli@unifi.it (N.C.)

⁴ Dipartimento Scienze Biologiche, Geologiche e Ambientali, Università di Bologna, P.zza Porta S. Donato 1, Bologna 40126, Italy; claudia.romagnoli@unibo.it

⁵ National Institute of Oceanography and Applied Geophysics—OGS, 34010 Trieste, Italy

* Correspondence: daniele.casalbore@uniroma1.it

Abstract: Stromboli is an active insular volcano located in the Southern Tyrrhenian Sea and its recent volcanic activity is mostly confined within the Sciara del Fuoco (SdF, hereafter), a 2-km wide subaerial–submarine collapse scar, which morphologically dominates the NW flank of the edifice. In August–November 2014, an effusive eruption occurred along the steep SdF slope, with multiple lava flows reaching the sea. The integration of multisensor remote sensing data, including lidar, photogrammetric, bathymetric surveys coupled with SAR amplitude images collected before and after the 2014 eruption enabled to reconstruct the dynamics of the lava flows through the main morphological changes of the whole SdF slope. Well-defined and steep-sided ridges were created by lava flows during the early stages of the eruption, when effusion rates were high, favoring the penetration into the sea of lava flows as coherent bodies. Differently, fan-shaped features were emplaced during the declining stage of the eruption or in relation to lava overflows and associated gravel flows, suggesting the prevalence of volcanoclastic breccias with respect to coherent lava flows. The estimated volume of eruptive products emplaced on the SdF slope during the 2014 eruption, accounts for about $3.7 \times 10^6 \text{ m}^3$, 18% of which is in the submarine setting. This figure is different with respect to the previous 2007 eruption at Stromboli, when a large lava submarine delta formed. This discrepancy can be mainly related to the different elevation of the main vents feeding lava flows during the 2007 eruption (around 400 m) and the 2014 eruption (around 650 m). Besides slope accretion, instability processes were detected both in the subaerial and submarine SdF slope. Submarine slope failure mobilized at least $6 \times 10^5 \text{ m}^3$ of volcanoclastic material, representing the largest instability event detected since the 2007 lava delta emplacement.

Keywords: lava delta; slope failure; repeated bathymetric surveys; digital elevation models; LiDAR; PLÉIADES; morphological monitoring



Citation: Casalbore, D.; Di Traglia, F.; Bosman, A.; Romagnoli, C.; Casagli, N.; Chiocci, F.L. Submarine and Subaerial Morphological Changes Associated with the 2014 Eruption at Stromboli Island. *Remote Sens.* **2021**, *13*, 2043. <https://doi.org/10.3390/rs13112043>

Academic Editor: Balázs Székely

Received: 28 March 2021

Accepted: 20 May 2021

Published: 22 May 2021

Publisher's Note: MDPI stays neutral with regard to jurisdictional claims in published maps and institutional affiliations.



Copyright: © 2021 by the authors. Licensee MDPI, Basel, Switzerland. This article is an open access article distributed under the terms and conditions of the Creative Commons Attribution (CC BY) license (<https://creativecommons.org/licenses/by/4.0/>).

1. Introduction

Stromboli is the north-easternmost island of the Aeolian Archipelago in the Southern Tyrrhenian Sea, representing the tip of a large, 3000 m-high volcanic edifice (Figure 1). Stromboli and Panarea volcanic edifices are part of a 45 km long volcanic area developed along a NE-SW regional extensional fault system (Figure 1b) above the thinned continental crust of the Calabrian Arc [1,2]. The evolution of Stromboli island occurred in the last 85 ka (apart from the older Strombolicchio edifice dated at about 200 ka) and can be divided in six main growth stages, with magmas ranging from calc-alkaline to potassic series, typical

of an arc-volcanic setting, whose formation can be related to the subduction of the Ionian crust beneath the Calabrian Arc ([2] and references therein).

The Stromboli edifice is characterized by a quasi-bilateral symmetry with respect to a tectonically controlled NE-SW axis (Figure 1c), which corresponds to the main orientation and distribution of dykes, eruptive fissures, secondary vents and active summit craters during most of the volcano evolution [1–3]. Dyke intrusion along this axis also promoted the development of recurrent lateral collapses along the NW and SE flanks of the volcano [2,4,5]. Specifically, multiple sectors collapses affected the NW flank of the edifice in the last 13 ka, the last of them likely occurred during medieval times, leading to the development of the Sciarra del Fuoco scar, SdF hereafter (Figure 1c) [2].

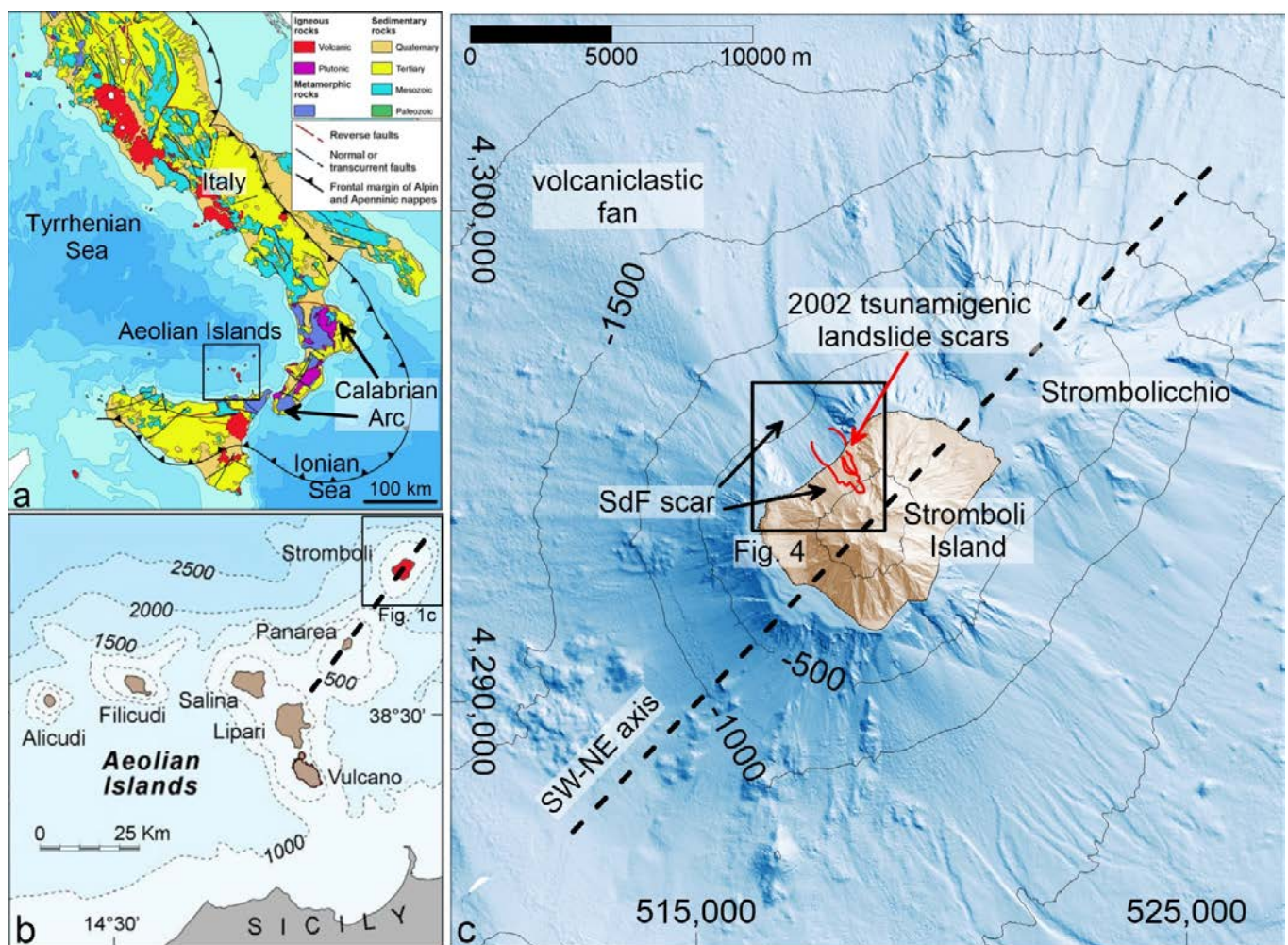


Figure 1. (a) Simplified geological map of Italy (modified from [6]), with the location of the Aeolian Islands (black box); (b) zoom of the Aeolian archipelago in the Southern Tyrrhenian Sea, with the geographical location of Stromboli Island (in red) and the main SW–NE regional system (black dashed lines) controlling the Stromboli–Panarea alignment; (c) shaded relief map and contour lines (equidistance 500 m) of the Stromboli edifice (location in Figure 1b), with the indication of the 2002 tsunamigenic landslide scars (see also Figure 4a) and the main rift axis oriented along the SW–NE direction.

The SdF is a very steep subaerial/submarine partially filled depression that funnels eruptive material produced at the summit craters into the sea, where a large volcanoclastic fan, composed by debris avalanche deposits and overlying turbidite deposits, is recognizable to over 3000 m water depth (mwd, hereafter) [7]. This volcanoclastic system is mostly fed by the persistent activity, occurring at the summit craters (South-Western, Central and North-Eastern Craters, SWC, CC and NEC, respectively, in Figure 1a). This activity, mostly consisting of low- to mid-energy Strombolian explosions, shows intensity and

frequency fluctuations over time and is punctuated by: (a) high-energy explosive events, called paroxysms [8,9], often associated with pyroclastic flows as observed in 2019 [10], and (b) lava overflows from the summit crater area [11,12] and/or effusive flank eruptions, as recently occurred in 1985–1986, 2002–2003, 2007 and 2014 [13–16].

Dyke intrusions and effusive eruptions also induce stress changes on the volcanic flanks and can generate slope instability at different spatial scales, as observed during the initial phases of the last four flank eruptions [16–18]. Of these events, only the 2002–2003 eruption was associated with the occurrence of tsunamigenic submarine and subaerial landslides (red dashed line in Figure 1c; [19,20]). The tsunami waves related to the 2002 submarine and subaerial landslides severely impacted the Stromboli coastline with a maximum runup of 10 m [21], evidencing the high hazard associated with similar events that have repeatedly occurred also during the previous century [22,23]. Since then, SdF slopes have been carefully monitored through repeated topographic surveys for their submarine [24–26] and subaerial part [27]. These surveys are part of a more complex monitoring network including: ground-based thermal infrared data [3]; infrasonic monitoring [28], seismic network [29], borehole strainmeters [10], dilatometric sensors [30], ground tiltmeters [31], plume and soil gas geochemical monitoring [32,33], two ground-based interferometric synthetic aperture radar sites [34] and satellite thermal monitoring [35]. However, except for the study of the 2002–2003 eruption and related tsunamigenic landslides [36], no comprehensive subaerial and submarine studies of the eruptive events occurring at SdF were performed until now.

In this paper, we present an integrated analysis of multisensor remote sensing data for the characterization of the morphological changes associated with the 2014 effusive eruption occurred at Stromboli volcano, during which lava flows entered the sea in the NW shallow offshore of the island. In detail, the bathymetric comparison between multi-beam surveys performed before and after the 2014 eruption have been integrated with lidar, photogrammetric and SAR amplitude images [16], aimed at fully understanding the morphological evolution of the SdF slope involved in this eruption. The integration of submarine and subaerial DEMs also allows one to estimate the volume of the eruptive products emplaced on the SdF slope during the 2014 eruption and compare it with the values previously estimated using satellite and ground based thermal observation [28,37], thus providing a crossvalidation of the two methodological approaches.

More generally, the results of this study are important to better understand the behavior and morphological evolution of lava flows penetrating into the sea, mainly in relation to the paucity of bathymetric monitoring of coastal areas during eruptive crisis [25,38], with observations mainly limited to the subaerial part of lava deltas [27,39,40] or scuba dives at water depth less than 50 m [41,42]. This is a very important issue considering the possible hazard associated with these events in active insular and coastal volcanoes.

2. The 2014 Eruption: Chronology and Subaerial Morphological Analysis

The 2014 effusive eruption began on the morning of 7 August 2014 and ended on 13 November 2014. The eruption was preceded by two months of more intense activity and anomalous values in geophysical and geochemical parameters [28,32,43], with stronger and more frequent Strombolian explosions, overflows from the crater terrace and small landslides along the subaerial SdF triggered by crater-rim collapse or by remobilization of volcanoclastic material by overflows (Figure 2a, [44]). The most frequent explosive activity and the lava overflows were generated mainly by the NEC, with the accumulation and remobilization of volcanoclastic material along the central part of the SdF [16,44]. On 6 August 2014, starting in the early afternoon, a series of overflows from the NEC area reached the sea. These events were associated with crater-rim collapse landslides that occurred in the same sector (Figure 2a; [16]). The actual onset of the eruption (between 3 and 5 a.m. UTC on 7 August 2014) was marked by the propagation of magma from the crater terrace towards the NEC, with the development of an eruptive fracture that fed a

lava vent at an altitude of 650 m above sea level, asl hereafter (Figure 2d,e) located 100 m lower than the crater terrace altitude.

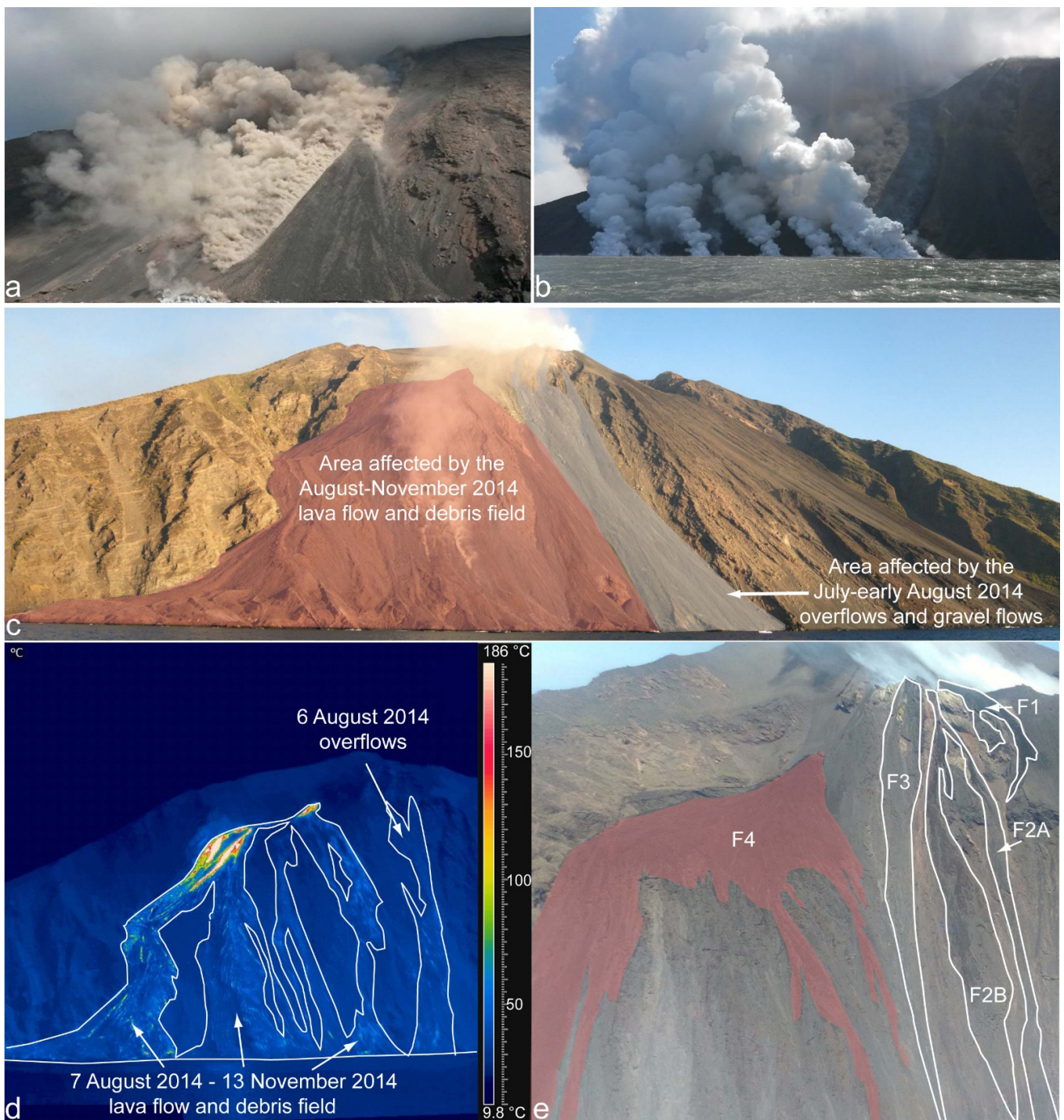


Figure 2. (a) Landslide associated with an overflow occurred on 6 August 2014; (b) initial phases of the 2014 eruption, with the entry into the sea of the various branches of the lava flow on 7 August 2014; (c) the Sciara del Fuoco during the 2014 effusion, with the extension of the 2014 lava field, the area affected by the different overflows of July-early August 2014 and by subsequent debris flows to November 2014; (d) single thermogram (approximately 0.67 m pixel resolution) showing the active lava flows, the various branches of the lava field, and the overflows of emplaced on 6 August 2014 and subsequent debris flows to November 2014; (e) proximal area of the upper SdF slope that highlights the emission zone of the July-early August 2014 overflows (F1 to F3) and the vent of the 2014 lava field (F4, in red).

The propagation of the fracture triggered the collapse of the volcanoclastic talus below the NEC [16]. The first days of the 2014 eruption were characterized by a high effusive rate, which decreased dramatically in the following days, and then remained low for the duration of the eruption [28,45]. During this initial phase, a series of lava flows reached the sea in different points, always located in the northernmost area of the SdF (Figure 2b–d; [46]). Subsequently, with the decrease of the effusive rate, the lava flows did not propagate far from the vent, with lava fronts that stood at around 400 m a.s.l.. This produced the typical morphology of Stromboli lavas with vent positioned at high altitudes [14], with the development of a proximal shield, a medial zone fed by small flows, and characterized by frequent lava crumbling down slope and producing a debris field, with debris moving downslope, to the coastline (Figure 2c,d; [46]).

The volume of lava emitted by the 2014 eruption has been estimated to be $7.4 \times 10^6 \text{ m}^3$ by [37] and $5.5 \times 10^6 \text{ m}^3$ by [28], with $2.697 \pm 0.190 \times 10^6 \text{ m}^3$ of lava emplaced on the subaerial slope (black dashed line in Figure 1b; [47]). After the 2014 eruption, at least for the period 2015–2016, the eruptive activity remained at very low levels [29], mainly characterized by sporadic, low intensity Strombolian explosions. In this period the volcanoclastic sedimentation from the crater area towards the SdF was significantly reduced, and erosion of the 2014 lava field mainly occurred, with small landslides mobilizing volumes in the order of 10^3 – 10^4 m^3 [34].

3. Data and Methods

Data used for this research mainly rely on the analysis of morphological changes detected by using high-resolution topo-bathymetric surveys collected before and after the 2014 eruption along the SdF collapse scar and time-lapse SAR (synthetic aperture radar) amplitude images collected between May and August 2014 (Figure 3 and Table 1).

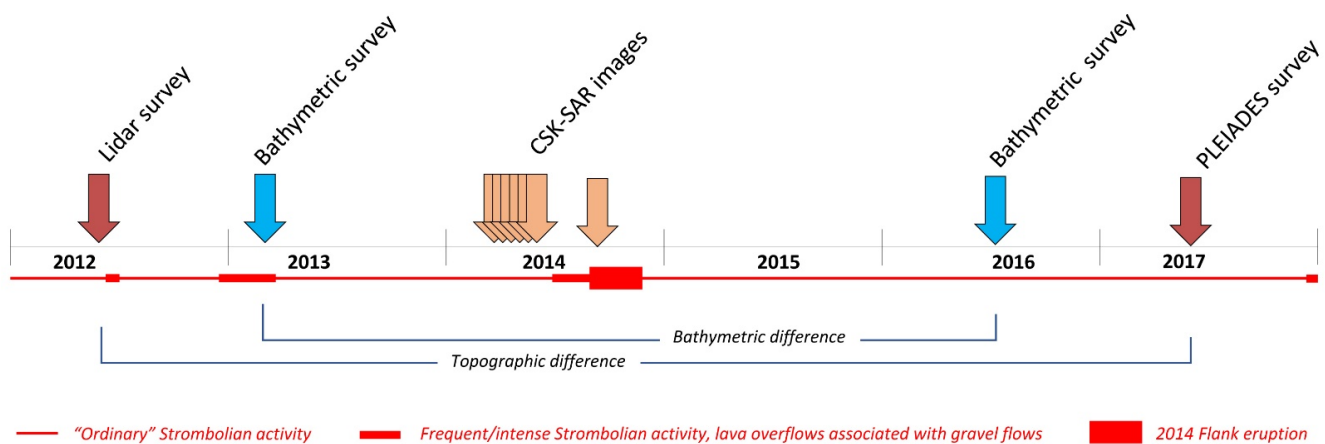


Figure 3. Timeline of the surveys performed for this study, with the indication of the 2014 flank eruption and period of “ordinary” and intense Strombolian activity.

Table 1. Timetable of the surveys used for monitoring the morphological evolution of the August–November 2014 effusive eruption at Stromboli. Time elapsed refers to months before (–) and after (+) the 2014 eruption.

Survey	Date	Time Elapsed	Elevation Range	Cell-Size
LiDAR	4–8/05/2012	–27 months	0–981 m a.s.l.	1 m
Bathymetry EM710 (70–100 kHz)	15/2/2013	–18 months	25–700 mwd	3 m
SAR amplitude COSMO-SkyMed	8/5/2014	–91 days	0–981 m a.s.l.	3 m
SAR amplitude	24/5/2014	–75 days	0–981 m a.s.l.	3 m

Table 1. Cont.

Survey	Date	Time Elapsed	Elevation Range	Cell-Size
SAR amplitude	9/6/2014	−59 days	0–981 m a.s.l.	3 m
SAR amplitude	25/6/2014	−43 days	0–981 m a.s.l.	3 m
SAR amplitude	11/7/2014	−27 days	0–981 m a.s.l.	3 m
SAR amplitude	27/7/2014	−11 days	0–981 m a.s.l.	3 m
SAR amplitude	12/8/2014	+5 days after the onset	0–981 m a.s.l.	3 m
Bathymetry Teledyne Reson 7125 (455 kHz) Teledyne Reson 8160 (45 kHz)	1/1/2016	+14 months	10–100 mwd 50–700 mwd	1–3 m
Photogrammetric PLÉIADES tri-stereo	26/05/2017	+30 months	0–981 m a.s.l.	1 m
CSK-SAR dataset description: COSMO-SKYMED				
Wavelength: 3.12 cm	Geometry: Descending	Sensor mode: H4-01	Track: 98	
Line of sight angles	25.48°	11.19°		
Line of sight versors	V: 0.903	N: −0.084	E: 0.422	

3.1. Lidar, Photogrammetric and Bathymetric Surveys

The difference map, obtained by comparing repeated digital elevation models (DEMs, hereafter), enable us to quantify the morphological change occurred on the SdF slope during the time interval between the surveys, with positive and negative values associated with slope accretion and erosion, respectively. The volumes associated with slope changes were obtained by integrating the difference in depth over the area of interest through the software Global Mapper. The reliability of computed volumes depends on the resolution and accuracy of the DEMs, as described below both for the submarine and subaerial slope.

For the submarine slope, seafloor changes were computed through the difference between multibeam bathymetries collected in 2013 and 2016 onboard the R.V. Urania and Minerva 1 (CNR). On 15 February 2013, bathymetric data were collected between 25 and 700 m water depths using the multibeam echosounder Kongsberg Simrad EM710 working at a frequency of 70–100 kHz. On 1 January 2016, bathymetric data were collected in the depth range 10–700 m using Teledyne Reson 7125 and 7160 multibeam echosounders working at a frequency of 400 kHz and 45 Hz in shallow- (<100 mwd) and deep-water (>100 mwd), respectively. In these surveys, data were DGPS-positioned and processed with hydrographic software (Caris Hips and Sips Professional), using daily sound speed profiles and patch test of transducers in the survey zone. Furthermore, a hull-mounted sound speed sensor was used to update in real-time the sound velocity values close to the flat face of the multibeam transducer. Tidal corrections were performed using data from the nearby tide gauge stations (www.mareografico.it). Random spikes and organized noise (multiple) produced by local very steep slopes were removed by applying geometrical and statistical filters. Cleaned multibeam data were gridded using a weighted averaging algorithm to produce the DEMs at variable resolution, from 1 m in shallow-water (<100 mwd) to 5 m at greater depths. DEMs used for bathymetric comparison were gridded with cell-size of 3 m and limited at depths <500 m, because at greater depths acoustic noise largely increased, making unreliable the computed changes. A vertical accuracy range of ± 0.5 m was estimated for the difference map by comparing the difference in depth of stable benchmarks between pairs of successive bathymetric sets. Small depth changes below this error range in the difference map were not considered in volume computations.

For the subaerial slope, topographic changes were estimated by comparing two DEM reconstructed starting from a LiDAR airborne survey (4–8 May 2012) and PLÉIADES-1 tri-stereo satellite imagery (26 May 2017). The LiDAR-DEM was obtained through the processing of the 3D point cloud that was acquired by using the Leica ADS80 sensor, which has

instrumental vertical and horizontal accuracy of 0.10–0.20 and 0.25 m, respectively [46,47]. The acquired point cloud has a mean point density of 8 pt/m². The 2017 DEM derived from the tri-stereo optical imagery acquired by the PLÉIADES-1 satellites, provided by Airbus with a nominal xy resolution of 1 m × 1 m. The PLÉIADES-1A (PHR1A) and PLÉIADES-1B (PHR1B) satellites can sense different synchronous images of the same area, with an angle variable between 6 and 28°. The tri-stereo approach consists of the acquisition of three nearly simultaneously images (one backward looking, one forward looking and a third near-nadir image) allowing the DEM reconstruction through the photogrammetric processing of the three stereo images [48]. Although the acquisitions used in this study are 100% cloud-free, the presence of the gas plume from the crater terrace prevented the reconstruction of the topography in this area. To assess the accuracy of the heights and their horizontal position in the PLÉIADES-1 DEM, ground control points (GCPs) were collected on the map database (cartographic XY standard deviation: 0.15 m). A block adjustment including all the satellite scenes was performed. The block adjustment was validated when the following accuracy was achieved: (i) an image's pixel xy bias smaller than 0.3 pixels, (ii) an image's pixel xy standard deviation smaller than 0.3 pixels and (iii) an image's pixel xy maximum residuals smaller than 2 pixels (for details see [16,47]). The z standard deviation was about 1.5 m (47).

3.2. Change Detection with SAR Amplitude Images

Data from SAR sensors have often been used to map areas that have been affected by lithological and morphological changes, i.e., to identify areas that have been impacted by eruptive and post-eruptive (landslides or floods) phenomena [49–51]. The SAR backscattering is determined by several factors, as the local morphology and the surface microrelief related to the grain-size, and the dielectric constant of the material at the surface [52,53]. To define which roughness scale affects the backscatter properties, the Rayleigh criterion was applied. In this way, the root mean squared height (hrms) variation on horizontal surfaces has been evaluated following [52] and, for the COSMO-SkyMed SAR (CSK-SAR) images used in this study, the hrms is approximately 4 mm. In an area with volcanoclastic sedimentation, this indicates that it is possible to identify the variation of the sedimented material between fine-grained (i.e., ash-dominated deposits) and coarse-grained (i.e., blocks and bombs dominated deposits, such as grain flows or 'a'ā lava surfaces). Local morphology produces irregularities having wavelengths at least twice as large as the satellite resolution cell due to changes in the local incidence angles, and it is not directly possible to separate the local morphology effects from the grain-size influence. Therefore, the term “roughness” is used to represent a combination of both factors [52].

To detect and interpret changes in land cover in connection with the SdF slope, RGB color composites are used [44,52]. The composite is created using these combinations:

- RED: 8 May 2014 image, considered as a reference for all the others;
- GREEN: image that is analyzed;
- BLUE: ratio of the amplitudes between the analyzed image and that of 8 May 2014.

The ratio is used because it depends on the relative average radar backscattering changes between two images, and therefore it does not depend on the pixel's intensity level [54].

A dataset comprising 7 COSMO-SkyMed SAR (CSK-SAR) images, acquired in descending orbit between 8 May 2014 and 12 August 2014, was used for this study (Figure 3 and Table 1). The products were coregistered, using the offset refinement based on the shuttle radar topography mission (SRTM) digital elevation model (DEM) at 1 arc second forming one unique stack, which is cropped around the target area. The cropped stack is geocoded by correcting SAR geometric distortions using SRTM DEM, producing SAR orthorectified map-projected images. Backscattered intensity of each image is transformed in amplitude image and then decibel scaled, converting the data into a virtual band with the expression $10 \cdot \log_{10}$ (amplitude). Finally, the quality of the images was enhanced using

a multitemporal speckle filter that reduces the “salt and pepper-like” texturing (speckle) of the CSK-SAR data.

4. Results

4.1. Morphological Evolution of the Submarine SdF between 2013 and 2016

The DEMs used to constrain seafloor changes associated with the August–November 2014 eruption were collected in February 2013 and January 2016, respectively (Figure 3). Despite the time gap before and after the eruption, our 20 years’ experience on submarine monitoring of the SdF has evidenced that the main morphological changes occur during eruptive crisis or increased period of Strombolian activity, while the “ordinary” evolution of the slope is limited to small readjustments of the shallowest part of the SdF [20,24–26].

The pre-2014 eruption submarine SdF slope can be morphologically divided in the SW and NE sectors, whose boundary roughly corresponds to the SW limit of the 2002 landslide scars (dashed red lines in Figure 4a). Considering also previous surveys, the SW sector in the time frame 2002–2017 was affected by minor morphological changes, whereas significant changes occurred in the NE sector both due to the morphological readjustment of the 2002 landslide scar, and to the emplacement of the 2007 lava delta (dotted blue lines in Figure 4a). These events left a depressed area in the southern part of the NE sector of the SdF slope, hereafter defined as the central part of the SdF.

The difference between pre- and post-2014 bathymetries shows that the main morphological changes on the NE sector of the SdF occur within the first 250 mwd, even if they locally extend down to 500 mwd (seaward limit of the difference map, Figure 4b). Seafloor accretion largely overwhelms erosion, accounting for a total estimated volume of $+1.75 \times 10^6 \text{ m}^3$ and $-3.5 \times 10^5 \text{ m}^3$, respectively (Table 2).

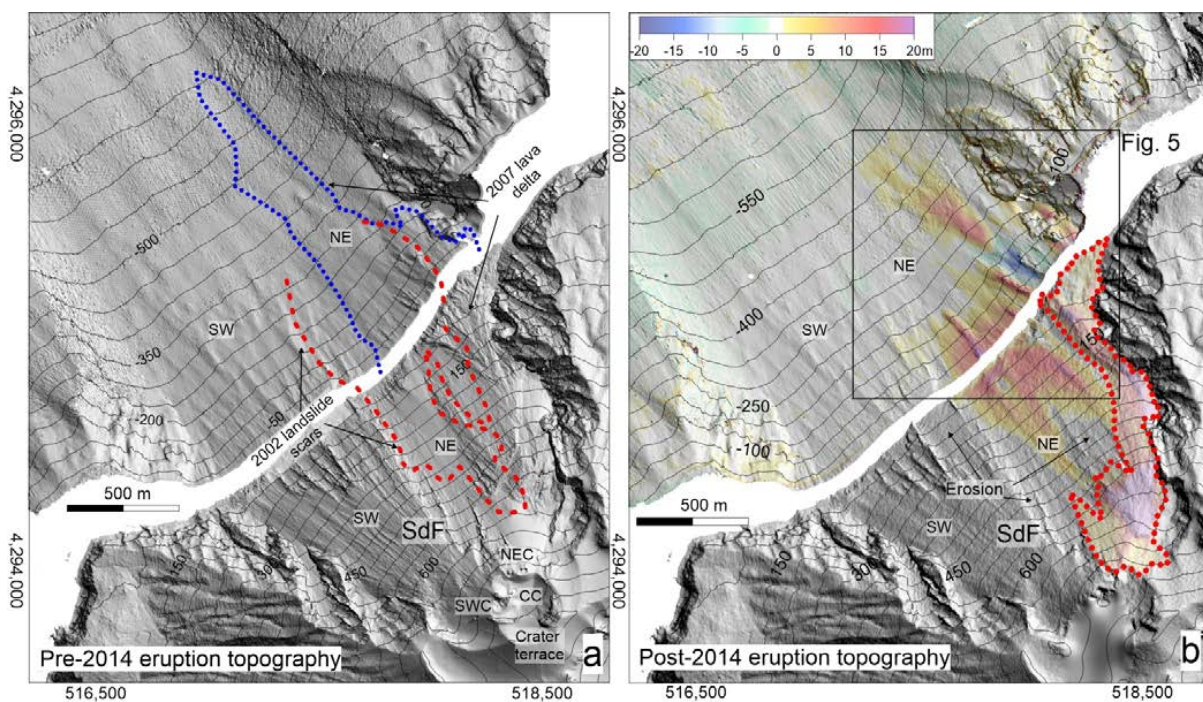


Figure 4. Shaded relief and contours (equidistance of 50 m) of the SdF in the NW Stromboli flank (location in Figure 1c), using (a) pre-2014 eruption topography, with the limits of the 2002 tsunamigenic landslides scars (dashed red lines) and the 2007 submarine lava delta (dotted blue line); (b) difference map (50% of transparency) between the pre- and post-2014 eruption topography, draped over the shaded relief and contours (equidistance of 50 m) of the SdF using post-2014 eruption DEM. The pre-/post-eruption comparison for the subaerial part of the SdF shows only accretion that largely overwhelms erosion (limited to a few sectors here indicated by arrows, see also (adapted from [47])). The dashed red line delimits the area with main morphological changes associated with the 2014 lava flows entering the sea.

Table 2. Volumetric estimation related to (a) submarine morphological changes (depth range 10–500 mwd) occurred between 2013 and 2106, (b) accretion and erosion of the entire SdF slope associated with the 2014 effusive eruption, (c) volcanoclastic material emplaced in the central part of the SdF, mainly before the 2014 eruption (see text for detail). The red and light-blue colors are referred to the subaerial and submarine flanks, respectively; the black color is used for the total volume. * Volume inferred in the gap area between the coastward limit of the bathymetric survey (around 10 mwd) and the coastline. Note that the error on z regard to the submarine and subaerial DEMs is on the order of 0.5 m and 1.5 m, respectively. The symbol \approx is used for approximately.

2013–2016 submarine morphological changes	Volume (m ³)
Seafloor accretion (10–500 mwd)	$\approx +1.75 \times 10^6$
Seafloor erosion (10–500 mwd)	$\approx -3.5 \times 10^5$
2014 Eruption (accretion and erosion)	Volume (m ³)
Main subaerial lava flows in the NE part of the SdF	$\approx 2.7 \times 10^6$
Subaerial lava flows in the central part of the SdF	$\approx 3.5 \times 10^5$
Total subaerial volume related to the 2014 eruption	$\approx 3.05 \times 10^6$
Seafloor accretion off the main lava flows (A2 and A3)	$\approx 3.3 \times 10^5$
Seafloor accretion in the central part of the SdF (A1)	$\approx 1.5 \times 10^5$
* Seafloor accretion inferred within the first 10 mwd	$\approx 2 \times 10^5$
Total submarine volume related to the 2014 eruption	$\approx 6.8 \times 10^5$
Total volume related to the 2014 eruption	$\approx 3.73 \times 10^6$
Main submarine landslide related to the 2014 eruption	$\approx -3.5 \times 10^5$
Submarine landslide deposits related to the 2014 eruption (A4)	$\approx 6 \times 10^5$
Volcanoclastic material in the central part of the SdF	Volume (m ³)
Volcanoclastic in the subaerial slope (first 500 m a.s.l.)	$\approx 1.35 \times 10^6$
Volcanoclastic in the submarine slope (10–250 mwd)	$\approx 4.9 \times 10^5$
* Volcanoclastic inferred in the submarine slope (<–10 mwd)	$\approx 2.1 \times 10^5$
Total volcanoclastic in the submarine slope	$\approx 7 \times 10^5$
Total volcanoclastic material in the SdF slope	$\approx 1.84 \times 10^6$

Seafloor erosion (light-blue area in Figures 4b and 5) was almost confined in an area of about 50,000 m² facing the central part of the 2007 lava delta between 20 (coastward limit of the bathymetric survey) and 200 mwd: here erosion affected the seabed up to 20 m of thickness (E1 area in Figure 5).

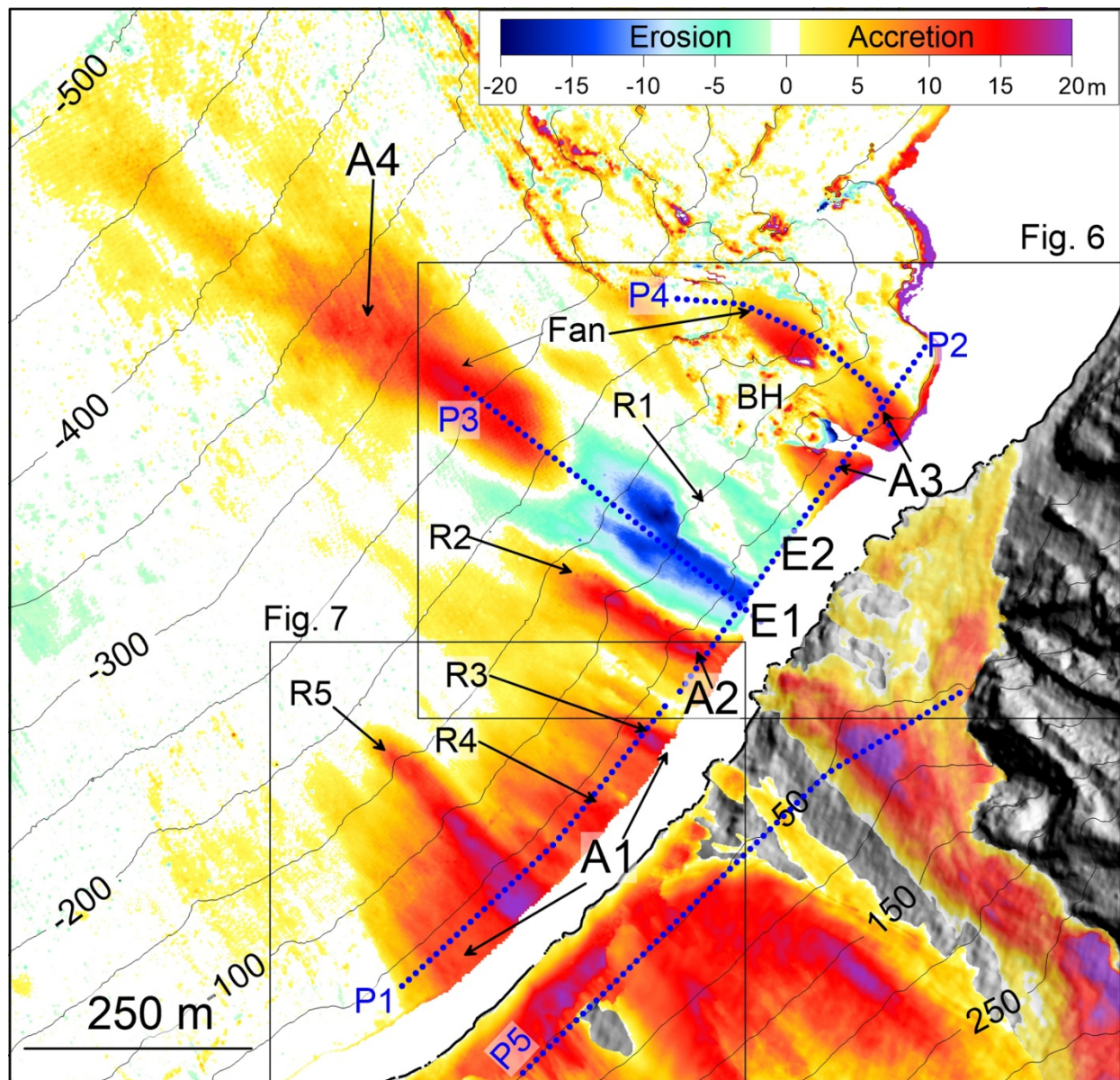


Figure 5. Zoom of the difference map between pre- and post-2014 eruption topography (location in Figure 4b, contours are derived from post-2014 eruption DEMs), with the indication of the main areas characterized by seafloor accretion (A1 to A4) and erosion (E1 and E2). Morphological ridges (R1 to R5) elongated downslope recognizable on the post-2014 bathymetry (Figures 6 and 7) and a previously existing basement high (BH) are also indicated, along with the trace of the bathymetric profiles (P1 to P5, blue dotted lines) shown in Figure 8.

A smaller erosive area (E2 in Figure 5), with thickness lower than 5 m, was recognizable just to the north of E1. These erosive areas correspond to the formation of channelized features on the 2016 DEM, bounded by steep-sided ridges (R1 and R2 in Figures 5 and 6b).

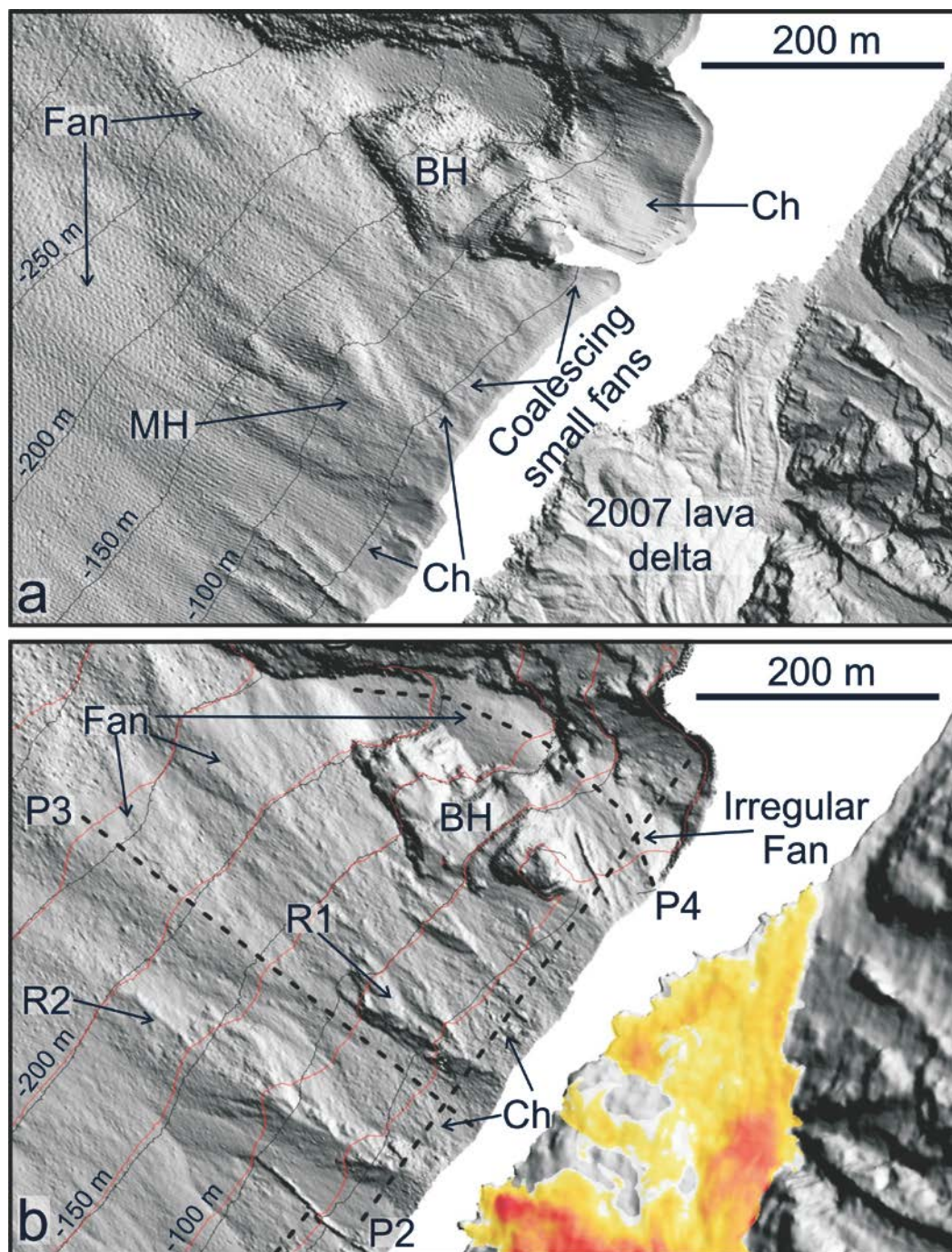


Figure 6. Zoom showing the (a) pre- and (b) post-2014 shaded relief and contours (black and red lines, respectively; equidistance 50 m) in the north-easternmost sector of the SdF collapse scar (location in Figure 5). In (b), the subaerial difference map between pre- and post-2014 eruption is also draped over the coastal topography (for the color scale refer to Figure 5) The dashed black lines (P2 to P4) are the trace of the bathymetric profiles shown in Figure 8. MH: morphological high; BH: basement high; R: ridge; Ch: channelized area.

The E1 channelized area (Figure 5 and Ch in Figure 6b) roughly matches the location of a large morphological high (MH in Figure 6a) on the 2013 DEM; the smaller E2 erosive area corresponds, instead, to an area previously characterized by small-scale coalescing fan-shaped features (Figure 6a).

Seafloor accretion, as resulting from the comparison between pre- and post-2014 eruption, can be divided in four main areas (A1–A4 in Figure 5): A1–A3 were mainly located in the first 200 mwd, while A4 was located at depths greater than 200 mwd.

The A4 area covers a surface of $1.8 \times 10^5 \text{ m}^2$ down to 500 mwd (seaward limit of the difference map) for a total estimated volume of $+6 \times 10^5 \text{ m}^3$; it morphologically corresponds to the development of a large fan-shaped feature, as visible on the 2016 DEM (Figure 6b), with its apex located within the E1 channelized area (see P3 in Figure 8).

The A1 area covers a surface of $1.25 \times 10^5 \text{ m}^2$, with a thickness of few tens of meters (Figure 5 and P1 in Figure 8) for a total estimated volume of $+8.35 \times 10^5 \text{ m}^3$; it morphologically corresponds to the development of small coalescing fan-shaped features alternated with downslope elongated ridges (R3, R4 and R5 in Figures 5 and 7b), characterized by a rough morphology and steep lateral gradients (over 60° , P1 in Figure 8) on the 2016 DEM.

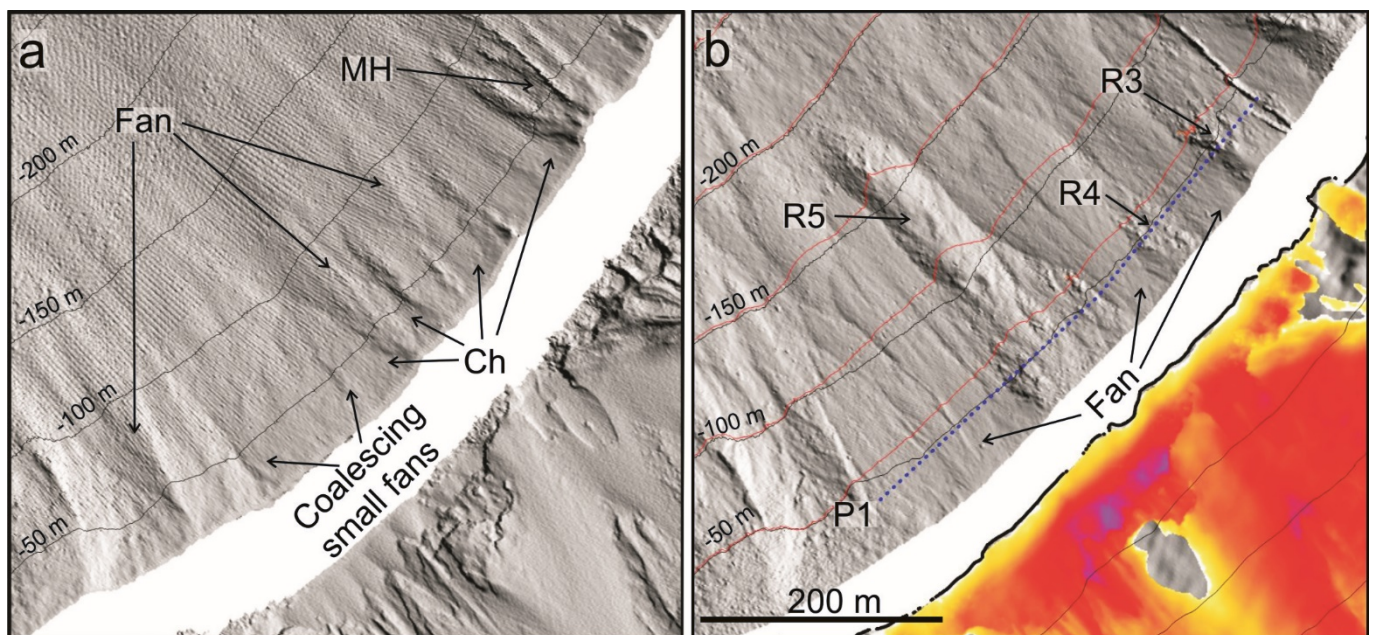


Figure 7. Zoom showing the (a) pre- and (b) post-2014 shaded relief and contours (black and red lines, respectively; equidistance 50 m) in the central sector of the SdF collapse scar (location in Figure 5). In (b), the subaerial difference map between pre- and post-2014 eruption is also draped over the coastal topography (for the color scale refer to Figure 5) The dashed blue line (P1) is the trace of the bathymetric profile shown in Figure 8. MH: morphological high; Ch: channelized area; R: ridge.

These ridges coincide, in fact, with the areas characterized by the highest values (up to 20 m) of seafloor accretion in A1 (Figure 5), mostly matching the location of previous channelized features (Ch in Figure 7a) recognizable on the 2013 DEM. The westernmost, main ridge (R5 in Figures 5 and 7b) extended down to 200 mwd for a length of 275 m, a width of 60 m and height of 5–6 m with respect to the surrounding seafloor (P1 in Figure 8).

The A2 accretion area also corresponded to a well-defined ridge (R2 in Figure 6b) on the 2016 DEM, having steep flanks (slope gradients up to 60° , P2 in Figure 8); this ridge extended over an area of $2.6 \times 10^4 \text{ m}^2$ down to 200 mwd, with a maximum thickness of 20 m (Figures 5 and 6b) for an estimated volume of $+1.7 \times 10^5 \text{ m}^3$. R2, together with smaller ridge (R1 in Figures 5 and 6b), bound the E1 erosive area. R2 was not present on the 2013 DEM, roughly matching the location of a previous channelized feature (Ch in Figure 6a), while R1 was already present before the eruption as part of a morphological high (MH in Figure 6a) and did not correspond to an accreted area in the difference map of Figure 5.

Finally, A3 was located in the NE-most part of the study area, covering a surface of $30,000 \text{ m}^2$ down to 200 mwd, with an average seafloor accretion of approximately 10 m (Figure 5 and P2 in Figure 8) for an estimated volume of about $+1.5 \times 10^5 \text{ m}^3$. Seafloor

accretion here morphologically corresponds to the development of irregular and smooth fan-shaped features on the 2016 DEM, developed above and below of a marked slope break (Figure 6b and P4 in Figure 8). These fan-shaped features were emplaced above a previous channelized feature recognizable on the 2013 DEM (Ch in Figure 6a), carving the NW flank of a basement high (BH in Figures 5 and 6) recognizable along the northern shoulder of the SdF collapse scar.

In order to compare submarine and subaerial morphological changes associated with the 2014 eruption, a topographic profile (P5 in Figure 8) crossing the entire NE sector of the SdF (location in Figure 5) is reported, showing the slope accretion occurred between 2012 and 2017 surveys.

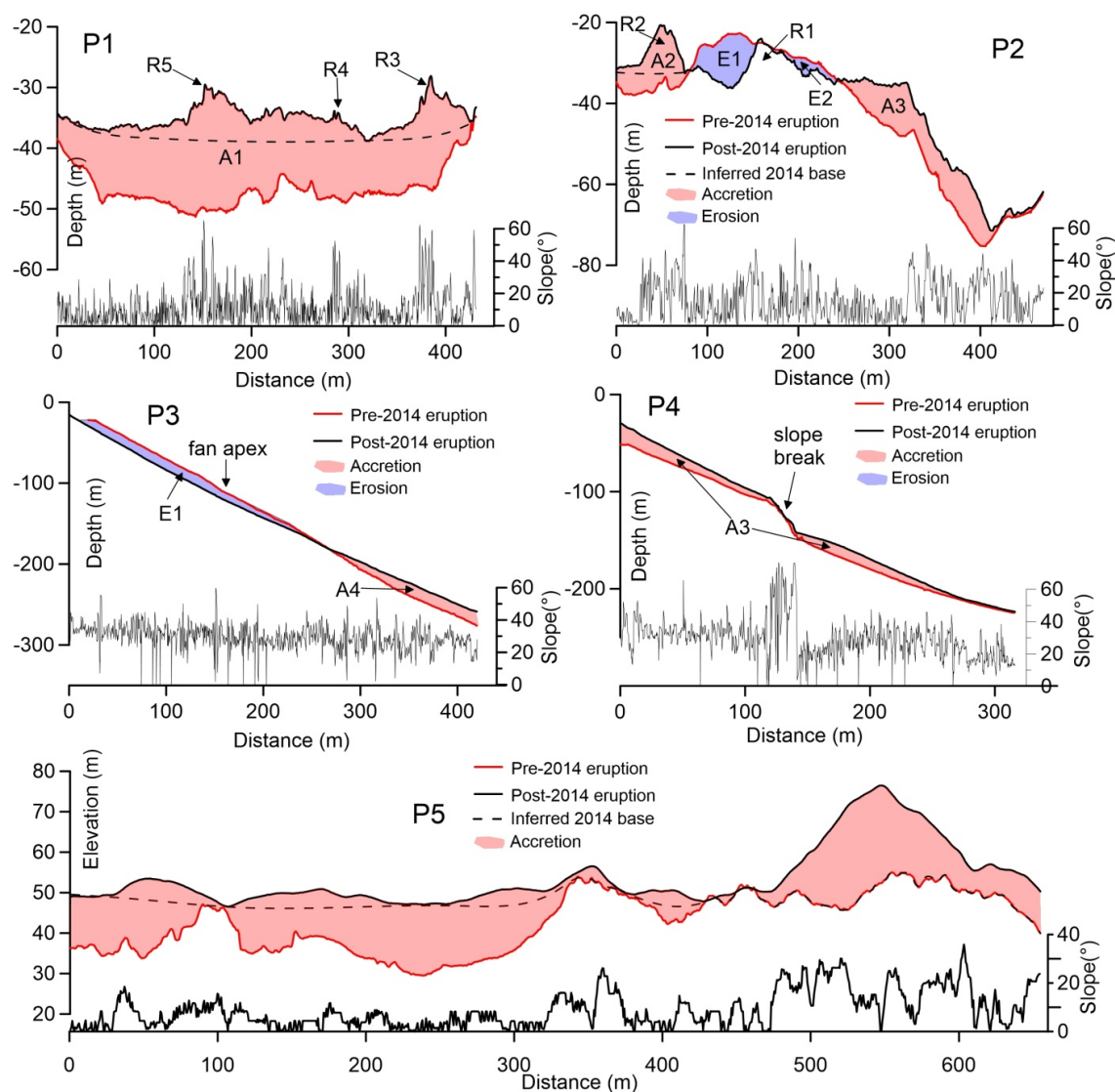


Figure 8. Bathymetric (P1–P4) and topographic (P5) profiles (location in Figures 5–7) showing seafloor accretion and erosion (red and light blue polygons, respectively) between pre- and post-2014 eruption topography. Acronyms as in the previous figures. Below the profiles, the graph of slope gradients is referred to the post-eruption topography. The location of the apex fan recognizable on the hillshade bathymetry of Figure 6b is reported on profile P3, indicating that the scar is partially filled by landslide deposits.

4.2. CSK-SAR Data Collected between May and August 2014

CSK-SAR images, collected between 8 May 2014 and 24 May 2014, show a decrease in the amplitude ratio (i.e., loss in SAR backscattering between the two consecutive images)

in the central portion of the SdF (Figure 9a), testifying the erosion of volcaniclastic deposits. Afterwards, the progressive increase in the explosion rate (16), and the emplacement of lava overflows and rock-falls evolving in gravel flows, produced the volcaniclastic sedimentation in the central part of the SdF (Figure 9b,c).

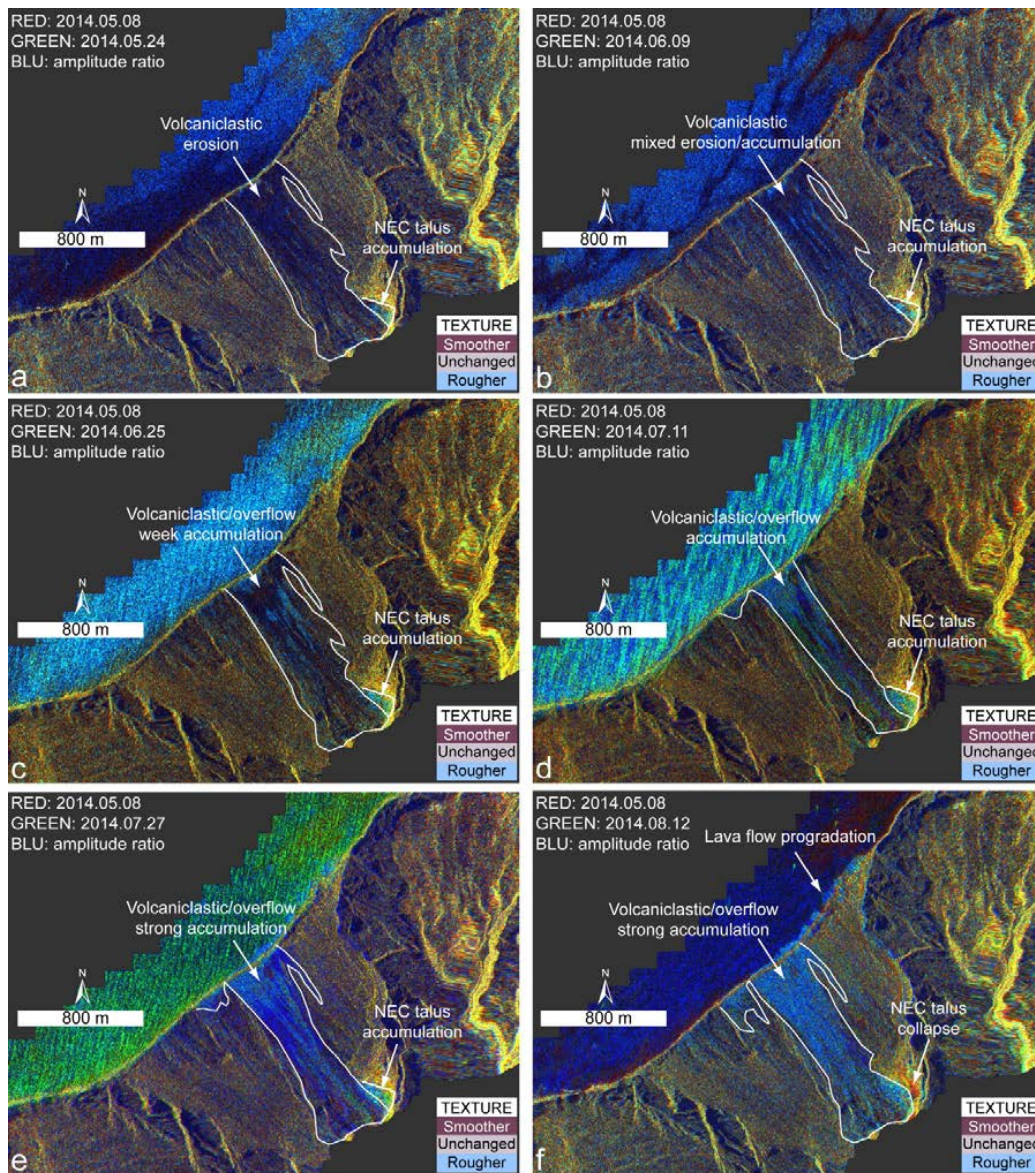


Figure 9. CSK amplitude RGB color composites (RED: 8 May 2014 amplitude image; GREEN: analyzed image; BLUE: ratio between the analyzed image and the 8 May 2014 image). For the significance given to “roughness” see the text. (a) comparison image between 8 May 2014 and 24 May 2014, with a reduction in the SAR amplitude in the central part of the SdF; (b) comparison image between 8 May 2014 and 9 June 2014, showing areas of reduced and increased SAR amplitude; in (c–e) it is possible to observe how the areas characterized by increased SAR amplitude increase over time (up to 27 July 2014). (f) The central area of the SdF is completely in shades of light blue, reflecting the increase of volcaniclastic sedimentation and overflows that occurred before the onset of the 2014 eruption. Note also the strong reduction of the SAR amplitude in the NEC talus area due to its collapse on 7 August 2014, while the 2014 lava field is characterized by little or no variation in the surface roughness.

This sedimentation (and related superficial roughness) clearly increased in the images collected before the onset of the eruption (11 and 27 July 2014; Figure 9d,e). The events of 6 August 2014, with a series of overflows associated with frequent landslides, significantly increased the roughness in the central part of the SdF (Figure 9f). In the same image,

the variation in amplitude on the coastline is due to the entrance into the sea of the lava flows. The lava effusion that began on 7 August 2014 instead produced no remarkable changes in SAR backscattered amplitude, probably due to the similar texture between the pre-effusive and the early-lava flows surfaces. Instead, it is possible to note how the area of proximal volcanoclastic accumulation (i.e., NEC talus) is characterized by accumulations during the whole period considered, except for the last image where an erosive process is highlighted (reduction in the backscattered amplitude in Figure 9f), consistent with the landslide occurred in the early stages of the eruption.

5. Discussion

5.1. Seafloor Accretion Associated with the 2014 Eruption

The seafloor accretion observed in areas A2 and A3 (Figure 5) fits well the entry points of the main lava flows reaching the sea on the NE-most sector of the SdF during the 2014 eruption (outlined by the dashed black lines in Figure 1b), emplaced above the remnants of the 2007 lava delta (Figure 6a; [16]). Once entered the sea, these lava flows built 40–60 m wide and some hundreds m long lobes (for instance R2 in Figure 6b), similarly to what was observed during the emplacement of the 2007 lava flows at Stromboli [25]. However, some morphological differences can be noted between the lobes emplaced in A2 and A3: while the former one corresponds to a well-defined and steep-sided ridge (R2 in Figure 6b), a more irregular, fan-shaped feature is present in the area A3 (see P2 in Figure 8 for comparison). This difference in morphology could be ascribed to the different amount of coherent lava flows with respect to chaotic breccias, using as reference the scuba observations made for the 2007 lava delta, where this kind of products were recognized [25]. Similarly, ancient analogous of ‘a’ā lava-fed deltas outcropping in Antarctica were found to be made up by the coalescence of “hyaloclastic lobes”, with variable percentages of coherent lavas and chaotic breccias [57].

The higher slope gradients (locally over 60°, P2 in Figure 8) observed along the flanks of R2 can be related to the high percentage of coherent lava flows forming this ridge. Lava flows feeding R2 were, in fact, active along the slope during the first days of the eruption, when the effusion rates were high (up to 20 m³/s according to the model of [28]). The high effusion rates can also justify the thicker accretion recognizable on the difference map in the coastal sector of the subaerial slope (red and violet colors in Figure 5 just above A2). Such conditions would have favored the penetration of lava flows into the sea as coherent bodies, as suggested by several laboratory and field studies [55,56]. On the meantime, the lower thickness observed for the 2014 lava flows in the coastal sector facing A3 (yellow colors in Figure 5) would justify the development of the irregular fan-shaped feature in this area, due to the prevalence of volcanoclastic breccias on the slope. The volcanoclastic contribution appeared predominant also moving downslope, where the emplacement of a smoothed fan is observed in A3, down to almost 200 mwd (Figure 6b). This composite fan likely formed during the declining stage of the 2014 eruption, when effusion rates reached a steady value of 0.4 m³/s, and the entrance of well-fed, coherent lava flows into the sea was no longer observed. Moreover, the steep slope break at around 100 mwd could have favored the brecciation of the less sustained submarine lava flows that reached this area, as testified by the thinned seafloor accretion over the slope break (see P4 in Figure 8).

The overall comparison between the pre- and post-bathymetries thus suggests a key role played by the paleomorphology of the SdF slope in controlling the location of the different lava flows and volcanoclastic lobes, which were emplaced within previous channelized features (Figure 6; P2 in Figure 8). Beyond the SW limit of the main 2014 lava flows (as reported by [16], indicated with the dashed line in Figure 4b), a series of steep-sided ridges (R3, R4 and R5 in Figures 5 and 7b) form the accretion area A1. From the comparison with onshore data (Figure 10) they can be interpreted as the submarine extension of lava flows that were mainly emitted during the first days of the 2014 eruption, when effusion rates were very high, and multiple flows reached this coastal sector (Figure 2b,d).

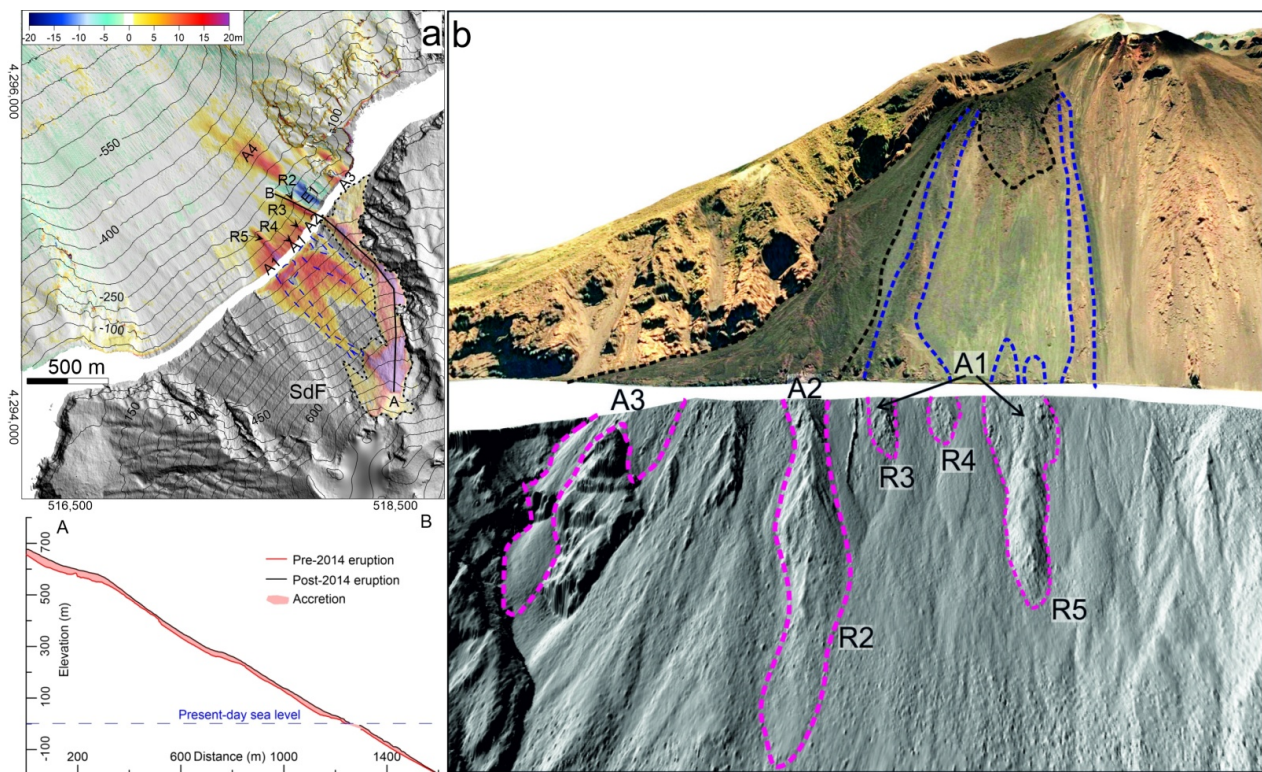


Figure 10. (a) Correlation between submarine and subaerial topographic changes, where A1–A4 are areas with seafloor accretion between 2012–2013 and 2016–2017; E1 is the main area with seafloor erosion during the same period. The profile A–B shows the slope accretion associated with the 2014 eruption along the main lava flows that characterized this eruption; (b) Main morphologies identified on the subaerial and submarine slope of the SdF; ridges R2 to R5 in magenta are compared with subaerial lava flows drawn as dashed blue lines associated with the 2014 eruption; see text for further details. Dashed black line on the subaerial SdF delimits the area with main morphological changes associated with the 2014 lava flows entering the sea from (adapted from [16]), whereas the blue dashed lines show the other subaerial ridges that in this study have been related to the 2014 lava flows through the integration of submarine/subaerial data.

Besides these ridges, the seafloor accretion in A1 is also made up of coalescing and overlapping small fan-shaped features (Figure 7b) that can be interpreted as the result of erosive-depositional processes associated with gravel flows entering the sea, fed by small-scale instabilities on the steep ($>30^\circ$) subaerial and submarine slope of the SdF. These small fan-shaped features are a common, but ephemeral feature, often observed in many bathymetric surveys performed since the 2002. They are associated with the morphological adjustment of the SdF slope that commonly occurs due to severe winter storms affecting the NW flank of the island. A good match is observed between subaerial and submarine accretion in the central sector of the SdF (Figures 5 and 10a), due to the progressive infilling of this depressed area (P1 and P5 in Figure 8). This infilling can be mainly related to the abundant volcanoclastic material derived from (a) overflow-induced landslides, (b) the NEC-talus collapse (Figure 2a) and (c) erosion of the upper part of the SdF (arrow in Figure 4b), occurred before, during and after the 2014 eruption.

CKS-SAR data show a relevant accumulation of volcanoclastic material within the depressed area encompassed between the 2007 lava delta and the SW limit of the 2002 landslide scar some months before the starting on the 2014 eruption (Figure 9). Differently, relatively mild slope dynamics, mainly characterized by weak erosive-depositional processes, occurred in the SdF in the period late 2014–early 2017 (Figure 3, [34]), when the post-2014 submarine/subaerial surveys were realized. A possible limit between the volcanic material emplaced in the submarine slope before and during the 2014 effusive eruption has been inferred by through the analysis of the bathymetric cross-sections by

reconstructing a hypothetical surface that approximately matches the base of the ridges before mentioned (R2 to R5, dashed black line indicated as “inferred 2014 base” in P1 and P2 of Figure 9).

5.2. Seafloor Erosion Associated with the 2014 Eruption

During the phase preceding the onset of the eruption, there were frequent gravel flows both from the edge of the crater terrace and along the SdF, mainly triggered by overflows. The volume of these gravel flows never reached 10^6 m³, remaining in the order of magnitude 10^4 – 10^5 m³ of remobilized material [16]. In the submarine slope, two failure events (E1 and E2 in Figures 5 and 10a) occurred where the main 2014 lava flows entered the sea, indicating a strong link between slope failures and 2014 eruptive dynamics. It is noteworthy that E1 is the larger submarine instability event recorded through the bathymetric monitoring along the SdF since the 2007 lava delta emplacement.

The computed volume of this event is around -3.5×10^5 m³ (Table 2), but this figure is very likely underestimated because: (a) bathymetric data are limited to water depth of 10 m, and the difference map indicates that the scar likely cuts back coastward and (b) the scar is partially filled both by landslides deposits in its distal part (see Figure 6b and P3 in Figure 8) and by small-scale fan-shaped features related to successive erosive-depositional process in its proximal part (Figure 6b). A more realistic estimate of the mobilized volume can be obtained by taking into account the A4 seafloor accretion area (Figures 4b, 5 and 10a), interpreted as the landslide deposits recognizable at the base of the scar and accounting for approximately $+6 \times 10^5$ m³ (Table 2). The low runout of the mobilized material is likely due to a rapid dissipation of pore pressures during the slide, similarly to what was reported for small submarine slope failures affecting the 2018 ‘a‘ā lava delta off Hawaii [38]. Again, this figure is likely underestimated because (a) the mapping of the landslide deposits is limited down to 500 mwd (Figure 5), and (b) the distal part of the moving landslide could be evolved downslope as sedimentary gravity flow, due to the steep gradients characterizing the SdF slope.

Regardless, the estimated volume of the E1 slope failure is two order magnitude larger than any instability processes occurred since the emplacement of the 2007 lava delta, and it also affected the more stable part of the delta according to the previous bathymetric surveys [26]. Such findings support our inference that triggering mechanisms for this larger slope failure are likely different from those common involved in the “ordinary” readjustment of the submarine slope, such as the loading of the 2014 lava flows on the submarine slope or the seismic activity associated with the 2014 eruptive event. However, the combined action of storm-waves cannot be excluded among the triggering mechanisms due to the shallow depths.

5.3. Volumetric Considerations on the 2014 Eruption and SdF Infilling

The estimation of the submarine volume emplaced during the 2014 eruption is difficult, because the subaerial and submarine surveys were not performed just after and before the eruption, as for instance realized during the 2007 eruption [15,25]. Data were collected one year before and one after the eruption for the submarine part and a slightly longer time frame (2012–2017) for the subaerial part. Despite such limits, some volumetric constraints on the overall material emplaced in the SdF during the 2014 eruption can be derived.

According to [16] the main lava flows emitted during the 2014 were emplaced in the NE-most sector of the SdF, encompassed by the dashed black line in Figures 1 and 9a, with a volume of approximately $+2.7 \times 10^6$ m³ (Table 2). Seafloor accretion in A2 and A3 (Figures 4b and 10) can be confidently associated with these lava flows, accounting for approximately $+3.3 \times 10^5$ m³ (Table 2). However, taking into account a southwestern, further extension of lava flows in the central part of the SdF on the base of submarine evidence (from R3 to R5 in Figures 5, 7, 8 and 10) we proposed in this work that further $+1.5 \times 10^5$ m³ can be added as products of the 7 August–13 November 2014 eruption (Table 2). Moreover, this figure is surely underestimated because the bathymetric com-

parison pre-/post-eruption is limited at depths greater than 10 m. In order to compute the volume not considered, an average thickness of 5 and 10 m has been assumed for the SW and NE sectors, respectively, based on the trend derived from the difference map and integrated over the coast. The estimated volume is $+2 \times 10^5 \text{ m}^3$ of material that added to the previous two figures accounts for a total estimated volume of $\approx 6.8 \times 10^5 \text{ m}^3$ in the submarine part of the SdF (Table 2).

A similar approach has been also applied for the central part of the subaerial SdF facing A1, where the volume possibly related to the 2014 eruption was distinguished with respect to the underlying volcanoclastic material by reconstructing a surface interpolated through the base of the subaerial ridges facing the submarine ones (P5 in Figure 8). This volume was estimated to about $+3.5 \times 10^5 \text{ m}^3$, which summed to the previous $+2.7 \times 10^6 \text{ m}^3$ accounts for a total volume of $+3.05 \times 10^6 \text{ m}^3$ emplaced on the subaerial slope (Table 2). It is noteworthy that the volume emplaced in the surveyed submarine area was markedly lower (about 5 times) than the volume emplaced on the subaerial SdF (Figure 11 and Table 2). This is different from what observed during the previous 2007 eruption, where the volume of the erupted material estimated for the submarine part (where a large lava delta in the order of $7 \times 10^6 \text{ m}^3$ of volume was formed, see [25]) was approximately three times larger than the subaerial one (Figure 11 and Table 2).

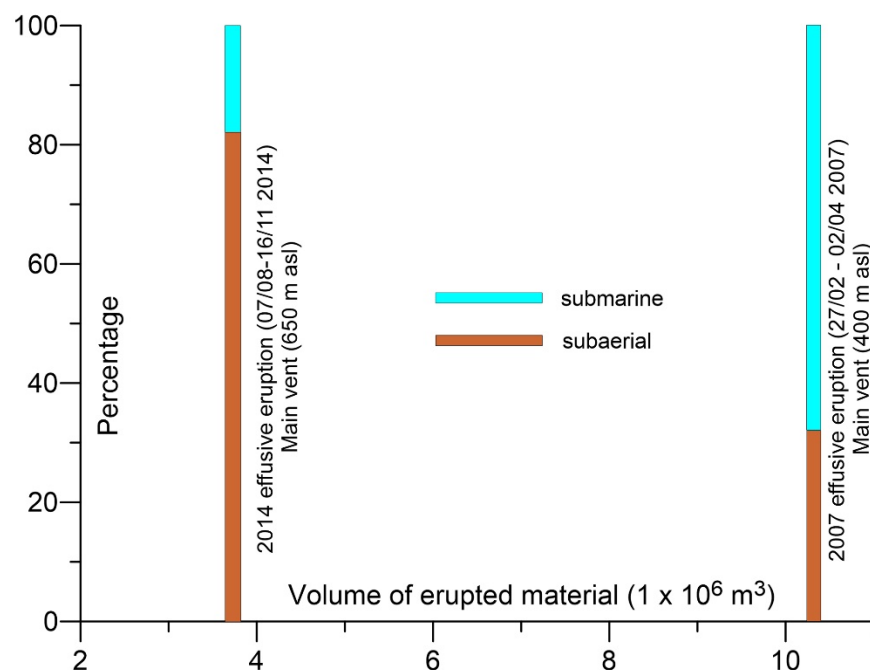


Figure 11. Bar graph showing the difference in volumes (see also Table 2) and percentages between volcanic material accreted on the subaerial (light brown) and submarine (light blue) slope of the SdF in correspondence of different eruptive phases.

This discrepancy can be mainly associated with the different elevation of the main vents feeding lava flows during the 2007 eruption (around 400 m a.s.l.) and the 2014 eruption (around 650 m a.s.l.). Considering that, during the 2014 eruption, effusion rates drastically fell from 20 to $0.5 \text{ m}^3/\text{s}$ just two days after the eruption [28], lava flows erupted by a high-elevation vent during the declining stage of the eruption could have remained mostly confined to the median part of the SdF slope, without reaching the sea. Another interesting finding is that the total volume estimated for the 2014 eruption through the above-described computations (approximately $+3.7 \times 10^6 \text{ m}^3$, Table 2) is markedly lower than the total bulk volume of $+7.4 \times 10^6 \text{ m}^3$ estimated using data derived by the new satellite Technology Experiment Carrier-1 (TET-1) [37], whereas it is more comparable to the total bulk volume of $+5.5 \times 10^6 \text{ m}^3$ obtained by thermal images from satellites using the

moderate resolution imaging spectroradiometer (MODIS) sensor [28]. This large difference can be mostly explained by the different methods used for constraining the total volume, as in the case of MODIS approach, where the error is usually estimated at 50% [58].

Nevertheless, our approach relies on topographic differences realized not contextually at the start and end of eruption, so hindering a clear discrimination between material the emplaced during the eruption with respect to the volcanoclastic material emplaced (mostly) before and after the eruption, especially in the central part of the SdF. This area, in fact, is a morphological low with respect to the surrounding NE and SW sectors, representing a main pathway for the funneling to the sea of volcanoclastic material produced by persistent strombolian activity and erosive processes acting in the upper SdF slope (Figures 4b and 10), and this makes difficult to discriminate between such deposits and the previous 2014 overflows. As a whole, our results show a good matching between the subaerial and submarine slope accretion in the central part of the SdF (Figures 4b, 5, 9 and 10a). As regards the subaerial slope, this infilling is mostly limited between 500 m and the coastline, resulting in a volume of approximately $+1.35 \times 10^6 \text{ m}^3$ (Table 2). For the submarine slope, the infilling is mostly limited down to -250 m , with an average accretion of 10 m for an estimated volume of approximately $+7 \times 10^5 \text{ m}^3$, $4.9 \times 10^5 \text{ m}^3$ of which were directly measured through the difference map (limited to depths greater than 10–15 m). The cumulative value between submarine and subaerial slope accounts for approximately $1.84 \times 10^6 \text{ m}^3$ accumulated during few years, representing not only eruptive dynamics but also gravity instability processes reworking the SdF slope. It is noteworthy that this infilling is also responsible for the development of a steep submarine volcanoclastic apron in the proximal sector of the submarine SdF that was one of the main factors controlling the geometry of the 2002 tsunamigenic landslide [20].

6. Conclusions

The integration of repeated bathymetric, lidar and photogrammetric surveys along with SAR amplitude images was a fundamental tool to understand the morphological evolution of the SdF slope induced by the 2014 eruption and its pre-eruptive stage, which was characterized by two months of intense Strombolian activity. Difference maps showed that slope accretion largely overwhelmed erosion along most of the SdF slope both before and during the 2014 eruption. The total volume of erupted material during the 2014 eruption was approximately estimated in $+3.7 \times 10^6 \text{ m}^3$, $\approx 80\%$ of which emplaced in the subaerial slope. This figure is different from what depicted for the previous 2007 eruption, where a large submarine lava delta formed, representing $\approx 75\%$ of the total volume. This difference can be explained by the location of the main vents feeding the 2007 (around 400 m a.s.l.) and 2014 eruption (around 650 m). Before the 2014 eruption, the total volume estimated is about $+1.84 \times 10^6 \text{ m}^3$, the 60% of which emplaced in the subaerial slope between 500 m and the coastline. The remaining 40% was emplaced in the submarine slope down to 250 mwd, promoting the formation of a steep volcanoclastic apron, a feature that increase the tsunamigenic potential of the SdF, as it was considered to have controlled the geometry of the submarine tsunamigenic landslide occurred in 2002.

The 2014 eruption also promoted significant slope instabilities along the SdF slope. In the subaerial slope, landslides mobilized volumes in the order of $-10^4/10^5 \text{ m}^3$, mostly affecting the upper part of the SdF during the early stages of the eruption. In the submarine slope, a main landslide scar was detected in the NE part of the SdF within the first 200 mwd, just off the entry points of the main 2014 lava flows. Landslide deposits are recognizable at the base of the scar, extending down to 500 mwd, corresponding to the limit of the bathymetric survey. This landslide mobilized a volume of at least $-6 \times 10^5 \text{ m}^3$, representing the largest slope failure affecting the submarine part of the 2007 lava delta since its emplacement.

DEM analysis also showed a good correlation between the subaerial and submarine slope and a variability in submarine morphologies associated with the entrance into the sea of lava flows (i.e., steep-sided ridges and fan-shaped features), reflecting a different ratio

between coherent lava flows and volcanoclastic breccias that, in turn, was likely controlled by changes in effusion rates and paleo-topography. This observation is very important for the interpretation of seafloor volcanic morphologies around insular and coastal volcanoes, mainly in relation to the paucity of marine studies monitoring the behavior of lava flows penetrating into the sea.

The presented results highlight the importance of integrated submarine and subaerial studies to monitor active volcanoes, providing a comprehensive view of the main processes (constructive vs destructive) associated with eruptive dynamics, with significant implications also for the related geohazard assessment.

Author Contributions: D.C. conceived and designed the study; A.B. and D.C. acquired and processed the multibeam data, D.C., F.L.C., C.R. and A.B. analyzed and interpreted the multibeam data; F.D.T. and N.C. analyzed and interpreted the topographic and CKS-SAR data; D.C., F.D.T. and C.R. led the writing of the main text, with the contribution of F.L.C. and A.B.; D.C., F.D.T. and F.L.C. prepared the figures. All authors have read and agreed to the published version of the manuscript.

Funding: This research was funded by the National Research Council and “Presidenza del Consiglio dei Ministri–Dipartimento della Protezione Civile” (Presidency of the Council of Ministers–Department of Civil Protection), through CNR-DPC and UniFi-DPC respective agreements, however, does not reflect the position and the official policies of the Department.

Data Availability Statement: The data presented in this study are available on request from the corresponding author. The data are not publicly available due to their acquisitional for institutional purposes.

Acknowledgments: Crew of R/V Urania and Minerva1 are gratefully acknowledged along with the people who took part in the surveys. This work was carried out using CSK[®] Products© ASI (Italian Space Agency), delivered under an ASI license to use in the framework of COSMO-SkyMed Open Call for Science (Project Id: 191; Project title: Volcano Instability—VITA; Scientific Coordinator: F. Di Traglia)”. The COSMO-SkyMed images were exploited from the COSMO-SkyMed data hub, managed by E-GEOS for ASI. The authors are grateful to E. Di Cuia (E-GEOS) for the technical support during the exploitation phase. X-band Cosmo-SkyMED images were processed using the freely delivered Sentinel Application Platform (SNAP) software. Three anonymous reviewers are gratefully acknowledged for their suggestions that improved the quality of the paper.

Conflicts of Interest: The authors declare no conflict of interest.

References

1. Bosman, A.; Chiocci, F.L.; Romagnoli, C. Morpho-structural setting of Stromboli volcano revealed by high-resolution bathymetry and backscatter data of its submarine portions. *Bull. Volcanol.* **2009**, *71*, 1007–1019. [[CrossRef](#)]
2. Francalanci, L.; Lucchi, F.; Keller, J.; De Astis, G.; Tranne, C.A. Chapter 13 Eruptive, volcano-tectonic and magmatic history of the Stromboli volcano (north-eastern Aeolian archipelago). *Geol. Soc. Lond. Memoirs* **2013**, *37*, 397–471. [[CrossRef](#)]
3. Calvari, S.; Bonaccorso, A.; Madonia, P.; Neri, M.; Liuzzo, M.; Salerno, G.G.; Behncke, B.; Caltabiano, T.; Cristaldi, A.; Giuffrida, G.; et al. Major eruptive style changes induced by structural modifications of a shallow conduit system: The 2007–2012 Stromboli case. *Bull. Volcanol.* **2014**, *76*, 1–15. [[CrossRef](#)]
4. Kokelaar, P.; Romagnoli, C. Sector collapse, sedimentation and clast population evolution at an active island-arc volcano: Stromboli, Italy. *Bull. Volcanol.* **1995**, *57*, 240–262. [[CrossRef](#)]
5. Romagnoli, C.; Casalbore, D.; Chiocci, F.L.; Bosman, A. Offshore evidence of large-scale lateral collapses on the eastern flank of Stromboli, Italy, due to structurally-controlled, bilateral flank instability. *Mar. Geol.* **2009**, *262*, 1–13. [[CrossRef](#)]
6. Bosellini, A. Outline of the Geology of Italy. In *Landscapes and Landforms of Italy*; Springer: Cham, Switzerland, 2017; pp. 21–27.
7. Romagnoli, C.; Kokelaar, P.; Casalbore, D.; Chiocci, F.L. Lateral collapses and active sedimentary processes on the northwestern flank of Stromboli volcano, Italy. *Mar. Geol.* **2009**, *265*, 101–119. [[CrossRef](#)]
8. Barberi, F.; Rosi, M.; Sodi, A. Volcanic hazard assessment at Stromboli based on review of historical data. *Acta Vulcanol.* **1993**, *3*, 173–187.
9. Bevilacqua, A.; Bertagnini, A.; Pompilio, M.; Landi, P.; Del Carlo, P.; Di Roberto, A.; Aspinall, W.; Neri, A. Major explosions and paroxysms at Stromboli (Italy): A new historical catalog and temporal models of occurrence with uncertainty quantification. *Sci. Rep.* **2020**, *10*, 17357. [[CrossRef](#)] [[PubMed](#)]
10. Giudicepietro, F.; López, C.; Macedonio, G.; Alparone, S.; Bianco, F.; Calvari, S.; De Cesare, W.; Donne, D.D.; Di Lieto, B.; Esposito, A.M.; et al. Geophysical precursors of the July-August 2019 paroxysmal eruptive phase and their implications for Stromboli volcano (Italy) monitoring. *Sci. Rep.* **2020**, *10*, 10296. [[CrossRef](#)]

11. Calvari, S.; Intrieri, E.; Di Traglia, F.; Bonaccorso, A.; Casagli, N.; Cristaldi, A. Monitoring crater-wall collapse at active volcanoes: A study of the 12 January 2013 event at Stromboli. *Bull. Volcanol.* **2016**, *78*, 39. [[CrossRef](#)]
12. Calvari, S.; Di Traglia, F.; Ganci, G.; Giudicepietro, F.; Macedonio, G.; Cappello, A.; Nolesini, T.; Pecora, E.; Bilotta, G.; Centorrino, V.; et al. Overflows and Pyroclastic Density Currents in March–April 2020 at Stromboli Volcano Detected by Remote Sensing and Seismic Monitoring Data. *Remote Sens.* **2020**, *12*, 3010. [[CrossRef](#)]
13. De Fino, M. The Stromboli eruption of 6 December 1985–25 April 1986: Volcanological, petrological and seismological data. *Rend. Soc. Ital. Mineral. Petrol.* **1988**, *43*, 1021–1038.
14. Lodato, L.; Spampinato, L.; Harris, A.; Calvari, S.; Dehn, J.; Patrick, M. The morphology and evolution of the Stromboli 2002–2003 lava flow field: An example of a basaltic flow field emplaced on a steep slope. *Bull. Volcanol.* **2007**, *69*, 661–679. [[CrossRef](#)]
15. Marsella, M.; Baldi, P.; Coltelli, M.; Fabris, M. The morphological evolution of the Sciara del Fuoco since 1868: Reconstructing the effusive activity at Stromboli volcano. *Bull. Volcanol.* **2011**, *74*, 231–248. [[CrossRef](#)]
16. Di Traglia, F.; Calvari, S.; D’Auria, L.; Nolesini, T.; Bonaccorso, A.; Fornaciai, A.; Esposito, A.; Cristaldi, A.; Favalli, M.; Casagli, N. The 2014 Effusive Eruption at Stromboli: New Insights from In Situ and Remote-Sensing Measurements. *Remote Sens.* **2018**, *10*, 2035. [[CrossRef](#)]
17. Bonaccorso, A.; Calvari, S.; Linde, A.; Sacks, S.; Boschi, E. Dynamics of the shallow plumbing system investigated from borehole strainmeters and cameras during the 15 March, 2007 Vulcanian paroxysm at Stromboli volcano. *Earth Planet. Sci. Lett.* **2012**, *357–358*, 249–256. [[CrossRef](#)]
18. Di Traglia, F.; Nolesini, T.; Intrieri, E.; Mugnai, F.; Leva, D.; Rosi, M.; Casagli, N. Review of ten years of volcano de-formations recorded by the ground-based InSAR monitoring system at Stromboli volcano: A tool to mitigate volcano flank dynamics and intense volcanic activity. *Earth Sci. Rev.* **2014**, *139*, 317–335. [[CrossRef](#)]
19. Tommasi, P.; Baldi, P.; Chiocci, F.L.; Coltelli, M.; Marsella, M.; Pompilio, M.; Romagnoli, C. The Landslide Sequence Induced by the 2002 Eruption at Stromboli Volcano. In *Landslides*; Springer: Berlin/Heidelberg, Germany, 2005; pp. 251–258.
20. Chiocci, F.L.; Romagnoli, C.; Tommasi, P.; Bosman, A. The Stromboli 2002 tsunamigenic submarine slide: Characteristics and possible failure mechanisms. *J. Geophys. Res. Solid Earth* **2008**, *113*. [[CrossRef](#)]
21. Tinti, S.; Pagnoni, G.; Zaniboni, F. The landslides and tsunamis of the 30th of December 2002 in Stromboli analysed through numerical simulations. *Bull. Volcanol.* **2006**, *68*, 462–479. [[CrossRef](#)]
22. Maramai, A.; Graziani, L.; Tinti, S. Tsunamis in the Aeolian Islands (southern Italy): A review. *Mar. Geol.* **2005**, *215*, 11–21. [[CrossRef](#)]
23. Fornaciai, A.; Favalli, M.; Nannipieri, L. Numerical simulation of the tsunamis generated by the Sciara del Fuoco landslides (Stromboli Island, Italy). *Sci. Rep.* **2019**, *9*, 1–12. [[CrossRef](#)] [[PubMed](#)]
24. Chiocci, F.L.; Romagnoli, C.; Bosman, A. Morphologic resilience and depositional processes due to the rapid evolution of the submerged Sciara del Fuoco (Stromboli Island) after the December 2002 submarine slide and tsunamis. *Geomorphology* **2008**, *100*, 356–365. [[CrossRef](#)]
25. Bosman, A.; Casalbore, D.; Romagnoli, C.; Chiocci, F.L. Formation of an ‘a’ā lava delta: Insights from time-lapse multibeam bathymetry and direct observations during the Stromboli 2007 eruption. *Bull. Volcanol.* **2014**, *76*, 1–12. [[CrossRef](#)]
26. Casalbore, D.; Passeri, F.; Tommasi, P.; Verrucci, L.; Bosman, A.; Romagnoli, C.; Chiocci, F.L. Small-scale slope instability on the submarine flanks of insular volcanoes: The case-study of the Sciara del Fuoco slope (Stromboli). *Int. J. Earth Sci.* **2020**, *109*, 2643–2658. [[CrossRef](#)]
27. Marsella, M.; Proietti, C.; Sonnessa, A.; Coltelli, M.; Tommasi, P.; Bernardo, E. The evolution of the Sciara del Fuoco subaerial slope during the 2007 Stromboli eruption: Relation between deformation processes and effusive activity. *J. Volcanol. Geotherm. Res.* **2009**, *182*, 201–213. [[CrossRef](#)]
28. Valade, S.; Lacanna, G.; Coppola, D.; Laiolo, M.; Pistolesi, M.; Donne, D.D.; Genco, R.; Marchetti, E.; Ulivieri, G.; Allocca, C.; et al. Tracking dynamics of magma migration in open-conduit systems. *Bull. Volcanol.* **2016**, *78*, 78. [[CrossRef](#)]
29. Giudicepietro, F.; Calvari, S.; Alparone, S.; Bianco, F.; Bonaccorso, A.; Bruno, V.; Caputo, T.; Cristaldi, A.; D’Auria, L.; De Cesare, W.; et al. Integration of Ground-Based Remote-Sensing and In Situ Multidisciplinary Monitoring Data to Analyze the Eruptive Activity of Stromboli Volcano in 2017–2018. *Remote Sens.* **2019**, *11*, 1813. [[CrossRef](#)]
30. Di Lieto, B.; Romano, P.; Scarpa, R.; Linde, A.T. Strain Signals Before and During Paroxysmal Activity at Stromboli Volcano, Italy. *Geophys. Res. Lett.* **2020**, *47*. [[CrossRef](#)]
31. Ripepe, M.; Donne, D.D.; Genco, R.; Maggio, G.; Pistolesi, M.; Marchetti, E.; Lacanna, G.; Ulivieri, G.; Poggi, P. Volcano seismicity and ground deformation unveil the gravity-driven magma discharge dynamics of a volcanic eruption. *Nat. Commun.* **2015**, *6*, 6998. [[CrossRef](#)]
32. Rizzo, A.L.; Federico, C.; Inguaggiato, S.; Sollami, A.; Tantillo, M.; Vita, F.; Bellomo, S.; Longo, M.; Grassa, F.; Liuzzo, M. The 2014 effusive eruption at Stromboli volcano (Italy): Inferences from soil CO₂ flux and 3 He/4 He ratio in thermal waters. *Geophys. Res. Lett.* **2015**, *42*, 2235–2243. [[CrossRef](#)]
33. Inguaggiato, S.; Vita, F.; Cangemi, M.; Calderone, L. Increasing Summit Degassing at the Stromboli Volcano and Relationships with Volcanic Activity (2016–2018). *Geoscience* **2019**, *9*, 176. [[CrossRef](#)]
34. Schaefer, L.N.; Di Traglia, F.; Chaussard, E.; Lu, Z.; Nolesini, T.; Casagli, N. Monitoring volcano slope instability with Synthetic Aperture Radar: A review and new data from Pacaya (Guatemala) and Stromboli (Italy) volcanoes. *Earth Sci. Rev.* **2019**, *192*, 236–257. [[CrossRef](#)]

35. Massimetti, F.; Coppola, D.; Laiolo, M.; Valade, S.; Cigolini, C.; Ripepe, M. Volcanic Hot-Spot Detection Using SENTINEL-2: A Comparison with MODIS–MIROVA Thermal Data Series. *Remote Sens.* **2020**, *12*, 820. [[CrossRef](#)]
36. Baldi, P.; Bosman, A.; Chiocci, F.L.; Marsella, M.; Romagnoli, C.; Sonnessa, A. Integrated subaerial-submarine morphological evolution of the Sciara del Fuoco after the 2002 landslide. In *The Stromboli Volcano: An Integrated Study of the 2002–2003 Eruption*. Available online: <https://agupubs.onlinelibrary.wiley.com/doi/10.1029/182GM15> (accessed on 21 May 2021).
37. Zakšek, K.; Hort, M.; Lorenz, E. Satellite and Ground Based Thermal Observation of the 2014 Effusive Eruption at Stromboli Volcano. *Remote Sens.* **2015**, *7*, 17190–17211. [[CrossRef](#)]
38. Soule, S.A.; Zoeller, M.; Parcheta, C. Submarine lava deltas of the 2018 eruption of Kilauea volcano. *Bull. Volcanol.* **2021**, *83*, 1–16. [[CrossRef](#)]
39. Mattox, T.N.; Mangan, M.T. Littoral hydrovolcanic explosions: A case study of lava–seawater interaction at Kilauea Volcano. *J. Volcanol. Geotherm. Res.* **1997**, *75*, 1–17. [[CrossRef](#)]
40. Poland, M.P.; Orr, T.R. Identifying hazards associated with lava deltas. *Bull. Volcanol.* **2014**, *76*, 1–10. [[CrossRef](#)]
41. Moore, J.; Phillips, R.L.; Grigg, R.W.; Peterson, D.W.; Swanson, D.A. Flow of lava into the sea, 1969–1971, Kilauea volcano, Hawaii. *GSA Bull.* **1973**, *84*, 537–546. [[CrossRef](#)]
42. Tribble, G.W. Underwater observations of active lava flows from Kilauea volcano, Hawaii. *Geology* **1991**, *19*, 633–636. [[CrossRef](#)]
43. Di Traglia, F.; Battaglia, M.; Nolesini, T.; Lagomarsino, D.; Casagli, N. Shifts in the eruptive styles at Stromboli in 2010–2014 revealed by ground-based InSAR data. *Sci. Rep.* **2015**, *5*, 13569. [[CrossRef](#)]
44. Di Traglia, F.; Nolesini, T.; Ciampalini, A.; Solari, L.; Frodella, W.; Bellotti, F.; Fumagalli, A.; De Rosa, G.; Casagli, N. Tracking morphological changes and slope instability using spaceborne and ground-based SAR data. *Geomorphology* **2018**, *300*, 95–112. [[CrossRef](#)]
45. Ripepe, M.; Pistolesi, M.; Coppola, D.; Donne, D.D.; Genco, R.; Lacanna, G.; Laiolo, M.; Marchetti, E.; Ulivieri, G.; Valade, S. Forecasting Effusive Dynamics and Decompression Rates by Magmatic Model at Open-vent Volcanoes. *Sci. Rep.* **2017**, *7*, 1–9. [[CrossRef](#)] [[PubMed](#)]
46. Di Traglia, F.; Nolesini, T.; Solari, L.; Ciampalini, A.; Frodella, W.; Steri, D.; Allotta, B.; Rindi, A.; Marini, L.; Monni, N.; et al. Lava delta deformation as a proxy for submarine slope instability. *Earth Planet. Sci. Lett.* **2018**, *488*, 46–58. [[CrossRef](#)]
47. Di Traglia, F.; Fornaciai, A.; Favalli, M.; Nolesini, T.; Casagli, N. Catching geomorphological response to volcanic activity on steep slope volcanoes using multi-platform remote sensing. *Remote Sens.* **2020**, *12*, 438. [[CrossRef](#)]
48. Bagnardi, M.; Gonzalez, P.J.; Hooper, A. High-resolution digital elevation model from tri-stereo Pleiades-1 satellite imagery for lava flow volume estimates at Fogo Volcano. *Geophys. Res. Lett.* **2016**, *43*, 6267–6275. [[CrossRef](#)]
49. Arnold, D.; Biggs, J.; Wadge, G.; Ebmeier, S.; Odbert, H.; Poland, M. Dome growth, collapse, and valley fill at Soufrière Hills Volcano, Montserrat, from 1995 to 2013: Contributions from satellite radar measurements of topographic change. *Geosphere* **2016**, *12*, 1300–1315. [[CrossRef](#)]
50. Arnold, D.W.D.; Biggs, J.; Anderson, K.; Vargas, S.V.; Wadge, G.; Ebmeier, S.K.; Naranjo, M.F.; Mothes, P. Decaying Lava Extrusion Rate at El Reventador Volcano, Ecuador, Measured Using High-Resolution Satellite Radar. *J. Geophys. Res. Solid Earth* **2017**, *122*, 9966–9988. [[CrossRef](#)]
51. Chaussard, E. A low-cost method applicable worldwide for remotely mapping lava dome growth. *J. Volcanol. Geotherm. Res.* **2017**, *341*, 33–41. [[CrossRef](#)]
52. Wadge, G.; Cole, P.; Stinton, A.; Komorowski, J.-C.; Stewart, R.; Toombs, A.C.; Legendre, Y. Rapid topographic change measured by high-resolution satellite radar at Soufriere Hills Volcano, Montserrat, 2008–2010. *J. Volcanol. Geotherm. Res.* **2011**, *199*, 142–152. [[CrossRef](#)]
53. Ebmeier, S.K.; Biggs, J.; Muller, C.; Avard, G. Thin-skinned mass-wasting responsible for widespread deformation at Arenal volcano. *Front. Earth Sci.* **2014**, *2*, 35. [[CrossRef](#)]
54. Rignot, E.J.; Van Zyl, J.J. Change detection techniques for ERS-1 SAR data. *IEEE Trans. Geosci. Remote Sens.* **1993**, *31*, 896–906. [[CrossRef](#)]
55. Carr, P.F.; Jones, B.G. The influence of palaeoenvironment and lava flux on the emplacement of submarine, near-shore Late Permian basalt lavas, Sydney Basin (Australia). *J. Volcanol. Geotherm. Res.* **2001**, *112*, 247–266. [[CrossRef](#)]
56. Gregg, T.K.; Fink, J.H. A laboratory investigation into the effects of slope on lava flow morphology. *J. Volcanol. Geotherm. Res.* **2000**, *96*, 145–159. [[CrossRef](#)]
57. Smellie, J.L.; Wilch, T.I.; Rocchi, S. ‘A’ā lava-fed deltas: A new reference tool in paleoenvironmental studies. *Geology* **2013**, *41*, 403–406. [[CrossRef](#)]
58. Coppola, D.; Laiolo, M.; Piscopo, D.; Cigolini, C. Rheological control on the radiant density of active lava flows and domes. *J. Volcanol. Geotherm. Res.* **2013**, *249*, 39–48. [[CrossRef](#)]